*Article*

# Electrospun Interconnected Bead-Like P2-Na$_x$Co$_y$Mn$_{1-y}$O$_2$ (x = 0.66, y = 0.1) Cathode Material for Stable Sodium-Ion Storage

Anupriya K. Haridas [1,2], Milan K. Sadan [1,3], Joo-Hyung Kim [1], Younki Lee [1,*] and Jou-Hyeon Ahn [1,4,*]

1   Department of Materials Engineering and Convergence Technology, Gyeongsang National University, 501 Jinju-Daero, Jinju 52828, Korea
2   Department of Engineering, King's College London, London WC2R 2LS, UK
3   Department of Chemical and Biological Engineering, University of Sheffield, Sheffield S1 3JD, UK
4   Department of Chemical Engineering, Gyeongsang National University, 501 Jinju-Daero, Jinju 52828, Korea
*   Correspondence: ylee@gnu.ac.kr (Y.L.); jhahn@gnu.ac.kr (J.-H.A.)

**Abstract:** The development of high-rate and long-cycle-life Na-based cathode materials, on par with the performance of commercialized lithium-based cathodes, is crucial to satisfy the recurring surge in energy demand. Here, we report an interconnected bead-like P2-type manganese-based oxide Na$_x$Co$_y$Mn$_{1-y}$O$_2$ (x = 0.66, y = 0.1) synthesized by electrospinning and subsequent heat treatment as a high-rate cathode material for sodium-ion batteries (SIBs). The employed strategy of one-dimensional morphological design with interconnected bead-like particles profusely enhances Na$^+$ diffusion pathways. This layered cathode material exhibits a stable and superior discharge capacity of 180.0 mAh g$^{-1}$ at 50 mA g$^{-1}$ compared to a bare cathode material synthesized via the sol–gel process. Further, a high capacity of 78.3 mAh g$^{-1}$ was achieved, maintaining excellent capacity retention of 85.0% even after 500 insertion/desertion cycles implying robust Na$^+$ storage properties. High-rate tests also revealed promising electrochemical performances at C-rates as high as 5000 mA g$^{-1}$, affirming the potential of this layered cathode material for high-rate Na$^+$ storage. Additionally, full SIBs assembled with a Na$_x$Co$_y$Mn$_{1-y}$O$_2$ (x = 0.66, y = 0.1) cathode and a carbon nanofiber (CNF) anode exhibited a high cycle performance, retaining 96.3 mAh g$^{-1}$ after 100 cycles at 300 mA g$^{-1}$.

**Keywords:** electrospinning; P2-layered transition metal oxide; cathode material; high-rate; sodium-ion batteries

## 1. Introduction

Lithium-ion batteries (LIBs) have been explored extensively over the past decade for electronic devices, electric vehicles, and energy storage systems owing to their high energy density, long cycle life, and extended safety [1,2]. However, the unconventional exploitation of lithium resources over the years has resulted in substantial price hikes and scarcity of lithium resources [3]. Recently, sodium-ion batteries (SIBs) have gained significant research interest as a promising alternative to lithium-ion batteries, especially for large-scale energy storage applications, despite their lower energy density [4]. The natural abundance and the associated low cost of sodium can efficiently compensate for the low energy density. Apart from that, the similarity in their mechanism of operation with that of the already established LIBs makes it easier for research translation to specific practical applications [5]. Nonetheless, a major challenge in SIBs is to design and explore electrochemically active materials that can accommodate the relatively larger size of Na ions.

A plethora of materials, including Prussian blue analogs [6,7], transition metal oxides, fluorides [8,9], and polyanion compounds [10,11], are currently being explored as

intercalation cathode materials in SIBs following the development path of LIBs. However, identifying earth-abundant, low-cost, and environmentally benign materials that can function as intercalation cathodes in SIB is a significant challenge. In this regard, sodium manganese oxide-based cathodes ($Na_xMO_2$ ($0 < x \leq 1$); M = transition metal: Ni, Co, Mn, Fe, Cr) with a layered structure built by sheets of edge-sharing $TMO_6$ octahedra have been of immense research focus recently [12,13]. These environmentally friendly and cost-effective layered oxides are generally classified as prismatic (P) and octahedral (O) based on the coordination of the $Na^+$ in the layered structure [14]. Further, the change in oxygen layer stacking in this class of materials gives rise to O3, P2, and P3 structural variants, as reported by Delmas et al. [15]. Among them, P2-type manganese-based oxide materials possess better structural stability and reversible capacity compared to their O3 counterparts [16,17]. However, apart from the sluggish $Na^+$ diffusion kinetics, phase transformations occur in these materials at higher potentials due to extensive deintercalation of $Na^+$ ions accompanied by the Jahn–Teller distortion and dissolution of $Mn^{2+}$ in the electrolyte, resulting in capacity fade with extended cycling [18]. To enhance the cycle life of P2-type manganese-based oxide materials, various research groups have actively demonstrated strategies such as reducing $Na^+$ diffusion pathways via nanostructuring, employing various synthesis methods, and stabilizing the crystal structure by incorporating metal-ion dopants [16,17,19,20]. Furthermore, doping suitable transition metal ions such as Fe, Ni, and Co in Mn-based layered oxides can enhance the structural stability and reduce the effect of the Jahn–Teller distortion of $Mn^{3+}$ in $Na_xMnO_2$. Co doping, in particular, can improve electrical conductivity and $Na^+$ diffusion [21,22]. The impact of morphological variations on cycle performance cannot be ruled out. For example, Butcher et al. investigated the cycling performance of the morphological variants of $Na_xCo_yMn_{1-y}O_2$ with 10% Co doping and reported better cycling properties and rate performance for hollow spheres compared to flakes [23]. Cheng et al. recently reported the impact of higher Co content in stabilizing the structural distortion generated by $Mn^{3+}$ [24]. However, the favorable effect of minimal Co doping to lower the Jahn–Teller distortion encountered during cycling is much more significant and offers a wide scope for further exploration. Interestingly, few investigations have been conducted to understand the correlation between structural and morphological variations on P2-type cathodes.

Electrospinning is a versatile method to synthesize one-dimensional (1D) nanostructures such as nanorods [25], nanowires [26], and nanofibers [27]. This versatile technique has been explored to generate electrode active materials and separators in energy storage applications [28–30]. Electrospinning-based cathode materials are widely investigated in LIBs [31,32]. However, unlike LIBs, reports on electrospun oxide-based cathode materials have been limited to date in the case of SIBs. Among them, reports on electrospinning-based layered P2-type $Na^+$ cathodes are scarce and, hence, have an immense scope for development and optimization. For example, Kalluri et al. reported P2-type $Na_{2/3}(Fe_{1/2}Mn_{1/2})O_2$ fibers with a high discharge capacity of 166 mAh g$^{-1}$ at the 0.1 C-rate, but the cyclability was limited to 80 cycles [19]. High-rate 1D $Na_{0.44}MnO_2$ nanofibers and nanorods with 69.5 mAh g$^{-1}$ were reported by Fu et al. with limited rate capability [33]. In a similar attempt, the work by Li et al. reported $Na_{0.53}MnO_2$ nanorods with a discharge capacity of 80 mAh g$^{-1}$ at the 8 C-rate, but with inadequate cycle performance [34]. Thus, P2-layered cathodes still have an excellent scope to achieve high rate capability and high cyclability with rational electrode design and engineering.

Inspired by the previous reports on P2-type manganese-based cathode materials that suggest the favorability of metal-ion doping and morphological variations for the structural stability and electrochemical performance, herein, we describe the synthesis of an interconnected bead-like P2-type $Na_xCo_yMn_{1-y}O_2$ (x = 0.66, y = 0.1) (NaCM-*iB*) cathode with partial Co doping. The unique one-dimensional morphology reported here arises from the straightforward electrospinning process and high-temperature calcination utilized for the synthesis. The evaluation of $Na^+$ storage properties of this 1D cathode material revealed a promising electrochemical performance. The Co doping strategy coupled with the

one-dimensional morphological design consisting of interconnected particles thoroughly enhances sodium-ion diffusion pathways. As a result, the P2-NaCM-*iB* cathode displayed a superior reversible capacity compared with the bulk flake-like cathode synthesized via a typical sol–gel process. The cathode material exhibited a high discharge capacity of 180.2 mAh g$^{-1}$ at 50 mA g$^{-1}$ and a stable cycle life (500 cycles), maintaining a discharge capacity of 78.3 mAh g$^{-1}$ at 1500 mA g$^{-1}$ with almost 85.0% capacity retention. High rate capability up to 5000 mA g$^{-1}$ was demonstrated, confirming fast Na$^+$ transfer/storage properties. Additionally, full SIBs assembled with the P2-NaCM-*iB* cathode and a carbon nanofiber (CNF) anode exhibited good cycle performance, retaining 96.3 mAh g$^{-1}$ after 100 cycles.

## 2. Materials and Methods

### 2.1. Materials

Polyvinyl pyrrolidone (PVP, average Mw = 13,000,000, Sigma Aldrich, St. Louis, MO, USA), sodium acetate (≥99%, Sigma Aldrich), cobalt acetate tetrahydrate (98%, Sigma Aldrich), manganese acetate tetrahydrate (≥99%, Sigma Aldrich), ethanol (99.5%, Duksan Chem. Co., Ltd., Ansan, Korea), and *N*-methylpyrrolidone (NMP, 99.5%, Samchun Pure Chem. Co., Ltd., Pyeongtaek, Korea) were used as received.

### 2.2. Synthesis of an Interconnected Bead-Like P2-Type Manganese-Based Oxide/C

The interconnected bead-like P2-type manganese-based oxide/C was synthesized via an electrospinning process. Typically, PVP was entirely dissolved in an ethanol/water mixture (12 wt%, 1:1 *w/v*) by stirring thoroughly overnight. Later, metal acetate precursors were dissolved in an ethanol/DI water mixture (1:1, *w/v*) in appropriate stoichiometric ratios to finally yield P2-type Na$_x$Co$_y$Mn$_{1-y}$O$_2$ (x = 0.66, y = 0.1). Typically, 0.7 g of sodium acetate, 0.1 g of cobalt acetate tetrahydrate, and 0.9 g of manganese acetate tetrahydrate were used to bring the total solid content in the electrospinning solution to about 30%. The Na precursor was added in excess (5 wt%) to compensate for the high temperature loss of alkali ions. The solution was degassed entirely before the electrospinning process. Subsequently, electrospinning was carried out with an applied voltage of 18 kV, the distance of 15 cm between the collector to the tip of the needle, a flow rate of 0.3 mL h$^{-1}$, and 28% humidity. The as-spun fiber mat (Figure S1) was separated from the aluminum current collector and stored under vacuum for a day to eradicate the moisture content completely. Two-stage calcination of the fibers was carried out at 400 °C for 5 h followed by 800 °C for 6 h at a slow ramp rate of 3 °C min$^{-1}$ to obtain the interconnected bead-like P2-type Na$_x$Co$_y$Mn$_{1-y}$O$_2$ (x = 0.66, y = 0.1), referred to as NaCM-*iB* hereafter. A pristine Co-doped P2-type manganese-based oxide with a flake-like morphology (NaCM-*f*) was also prepared via a sol–gel process for comparison purposes as reported elsewhere, maintaining a similar stoichiometric ratio of elements in the final product [22].

### 2.3. Material Characterization

The morphology of the prepared composites was analyzed using a field emission scanning electron microscope (FE-SEM, Philips XL30S FEG) operated at 15 kV and a transmission electron microscope (TEM, TF30ST-300 kV). The crystal structure of the samples was investigated by X-ray diffraction (XRD) using a D2 Phaser Bruker AXS with a Cu K$\alpha$ X-ray source. The Rietveld refinement of the samples was carried out using FullProf in Match! The surface chemical properties of the samples were elucidated by carrying out X-ray photoelectron spectroscopy of the samples using XPS, ESCALAB250 VG Scientific, with a monochromatic Al K$\alpha$ 1486.6 eV X-ray source. The molar ratios of the metal ions in the synthesized samples were estimated with an inductively coupled plasma (ICP) spectrometer (Perkin Elmer, Optima 4300 DV). The carbon content in the sample was determined using an elemental analyzer (Flash 2000 Series, Thermo Fisher Scientific, Bremen, Germany).

### 2.4. Electrochemical Characterizations

The active materials (both P2-NaCM-*iB* and P2-NaCM-*f*) were mixed with a binder (PVDF) and a conductive agent (Super P) in an 8:1:1 ratio using NMP as the solvent. The viscous slurry was cast on an Al current collector and dried in a vacuum atmosphere at 100 °C for 10 h to remove the residual solvent. Later, circular 1 cm$^2$ disks were punched with active material loading of $1.5 \pm 0.2$ mg and employed as working electrodes. Both Swagelok-type cells and 2032 coin cells were utilized for battery testing. Half cells were assembled using either NaCM-*iB* or NaCM-*f* as the working electrode. The cells were assembled in an argon-filled glove box ($H_2O$ and $O_2$ content less than 1 ppm) with freshly cut sodium metal as the counter electrode and a Whatman GF/D glass fiber as the separator. $NaClO_4$ salt (1 M) dissolved in a mixture of ethylene carbonate (EC) and propylene carbonate (PC) (1/1, *vol/vol*) with 5 wt% fluoroethylene carbonate (FEC) was utilized as the electrolyte. For post-cycling analysis, the cells were disassembled inside the glove box, and the cathodes were carefully washed in EC and dried under vacuum conditions. A carbon nanofiber (CNF) electrode was prepared in-house and paired with the NaCM-*iB* cathode for full-cell studies. The preparation of the CNF electrode is detailed in the Supporting Information. The anode-to-cathode active material ratio was maintained at 1:4 to ensure capacity matching in the full cells. All the electrochemical tests in this study were carried out using an electrochemical workstation (WBCS 3000, WonA Tech. Co., Seoul, Korea). Specifically, cyclic voltammetry (CV) analysis and galvanostatic charge/discharge (GCD) studies were performed within the voltage range of 1.5 V to 3.9 V to avoid unwarranted structural changes during cycling. Electrochemical impedance spectroscopy (EIS) studies were conducted using an IM6 impedance analyzer in the frequency range from 100 kHz to 2 mHz at a signal amplitude of 5 mV.

## 3. Results and Discussion

The interconnected bead-like P2-type manganese-based oxide/C was synthesized via a simple electrospinning process utilizing metal precursors and a polymer solution. The scheme of the synthesis procedure is shown in Figure 1. Mn- and Co-based metal acetate precursors were initially dissolved in an ethanol/water mixture, maintaining stoichiometric ratios of Mn and Co. As the high-temperature volatilization of alkali metals is widely known, an additional Na precursor (8%; more than that of the stoichiometric amount) was added to compensate for the high temperature loss of Na. The mixture was stirred with an 12 wt% PVP solution until entirely homogeneous. The resultant solution was loaded into a syringe and subjected to electrospinning. The application of a specified voltage at a typical flow rate, temperature, and humidity led to the Taylor cone formation at the tip of the needle, which elongated, resulting in the formation of aligned fibers across the rotating mandrel collector. The voltage, flow rate, temperature, humidity, and distance from the collector to the tip of the needle for the electrospinning process were optimized to be 18 kV, 0.3 mL h$^{-1}$, 25 °C, 28%, and 15 cm, respectively. The digital photograph of the as-spun nanofiber mat is given in Figure S1. The as-spun fibers were uniform in size (Figure 2a,b), with an approximate fiber diameter of ~150 nm.
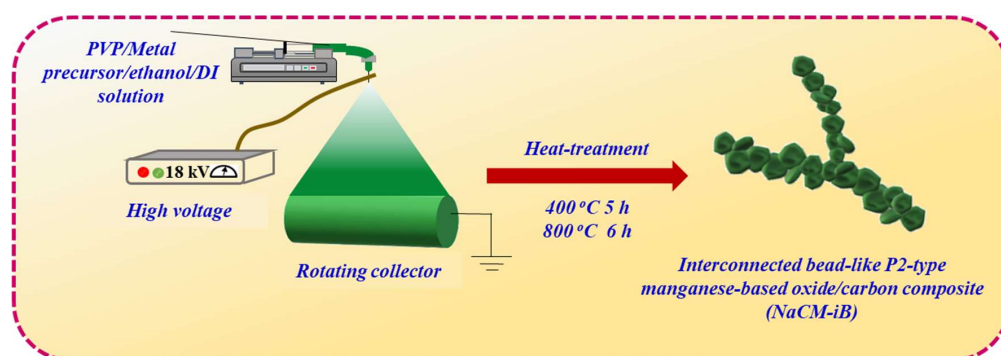


**Figure 1.** Schematic illustration of the synthesis of the NaCM-*iB* cathode material.
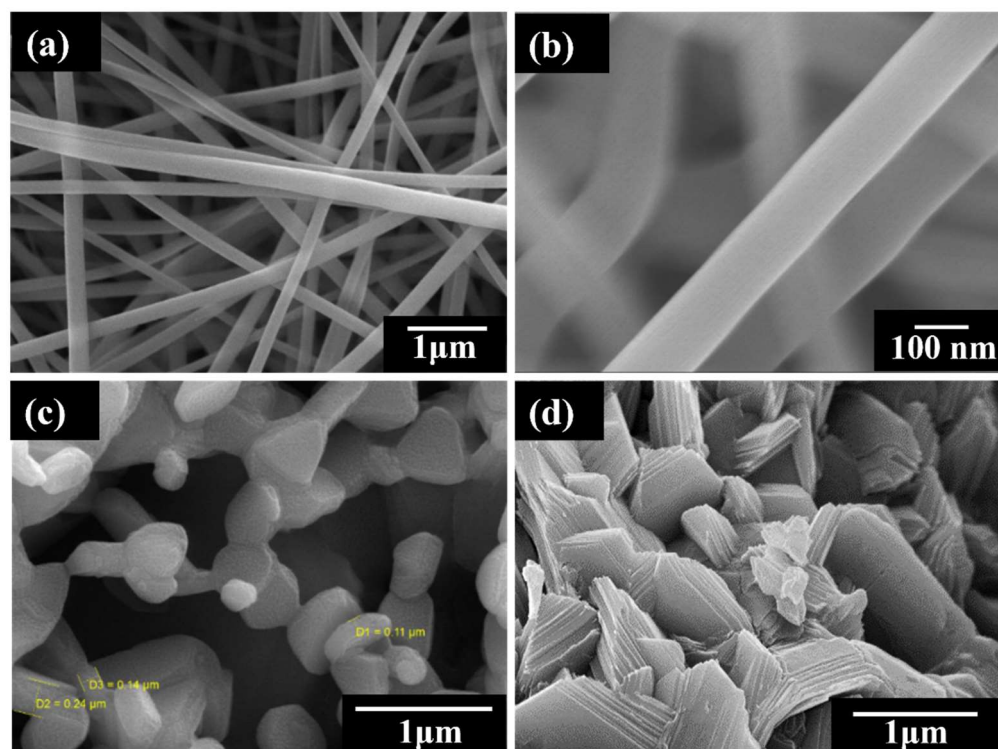
**Figure 2.** FESEM images of the (**a**,**b**) as-spun NaCM-*iB* nanofibers, (**c**) NaCM-*iB*, and (**d**) NaCM-*f* composites obtained after high temperature calcination.

Later, the obtained nanofibers were peeled off and heat-treated at 400 °C for 5 h to stabilize the fiber mat, which was followed by the second stage of heat treatment at 800 °C for 6 h in a compressed air atmosphere. A slow ramp rate of 3 °C min$^{-1}$ was employed throughout the entire heat treatment process to avoid the breakage of the nanofibrous morphology. The high-temperature heat treatment process led to the nucleation and growth of $Na_xCo_yMn_{1-y}O_2$ particles to form one-dimensional nanofibers and the simultaneous decomposition of the polymer PVP, leading to the formation of an interconnected bead-like structure, as shown in Figure 2c. The elemental mapping of the composite (Figure S2) demonstrates the distribution of the elements Na, Co, Mn, and O along the interconnected bead-like structure. However, in the case of the NaCM-*f* cathode, the metal acetate precursors chelated in the presence of citric acid during the sol–gel process to form a viscous gel. Upon the high-temperature heat treatment process, the nucleation and growth of the $Na_xCo_yMn_{1-y}O_2$ particles resulted in a flake-like morphology, as shown in Figure 2d. The elemental mapping of the NaCM-*f* composite is provided in Figure S3.

Rietveld-refined XRD patterns of the NaCM-*iB* and NaCM-*f* cathodes assuming the formation of a P63/mmc space group are presented in Figure 3a,b. The patterns exhibited identical high-intensity diffraction peaks for both the NaCM-*iB* and NaCM-*f*, indicating the formation of pure-phase $Na_xMnO_2$ in good agreement with JCPDS card number 27-0751. No additional impurity peaks were detected, denoting successful Co doping. However, a small amorphous peak was observed in the NaCM-*iB* from 20° to 25°, indicating the presence of amorphous carbon due to the incomplete decomposition of the encapsulating polymer material [35]. The refined structural parameters of the samples are presented in Table S1, indicating the size-induced minor enlargement in d spacing in the NaCM-*iB* sample.
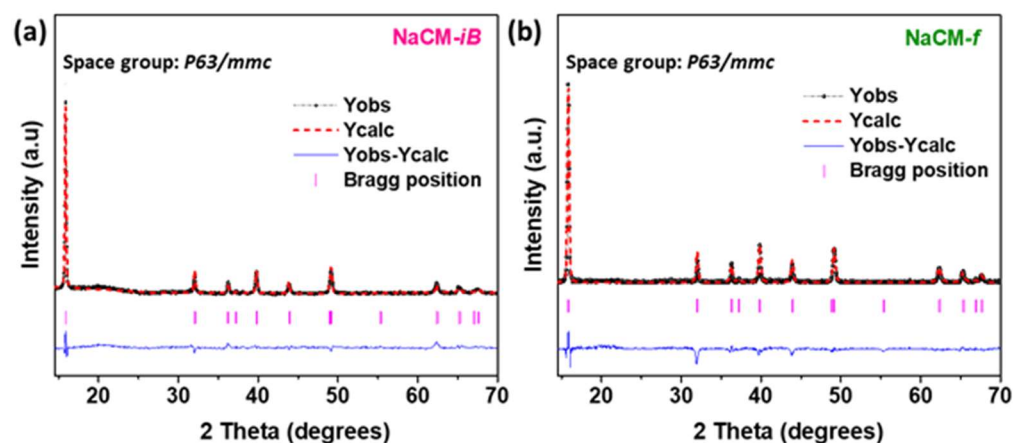
**Figure 3.** Rietveld-refined patterns of the (**a**) NaCM-*iB* and (**b**) NaCM-*f* samples.

Further structural analysis using TEM revealed the interconnected bead-like structure of the NaCM-*iB* and the hexagonal flake-like structure of the NaCM-*f* (Figure 4a,b). Clear lattice images of the NaCM-*iB* were not observed in HRTEM, indicating the presence of an amorphous carbon layer encapsulating the NaCM-*iB* composite (Figure 4c). However, the HRTEM image of the NaCM-*f* revealed a lattice spacing of 0.123 nm (Figure 4d) corresponding to the (002) plane consistent with the XRD pattern. The stoichiometric composition of the samples was estimated to be $Na_{0.66}Co_{0.09}Mn_{0.91}O_2$ and $Na_{0.66}Co_{0.13}Mn_{0.87}O_2$ based on the results of ICP analysis (see Table S2). Additionally, the amount of carbon in the NaCM-*iB* sample was estimated to be 2% by means of elemental analysis (Table S3).
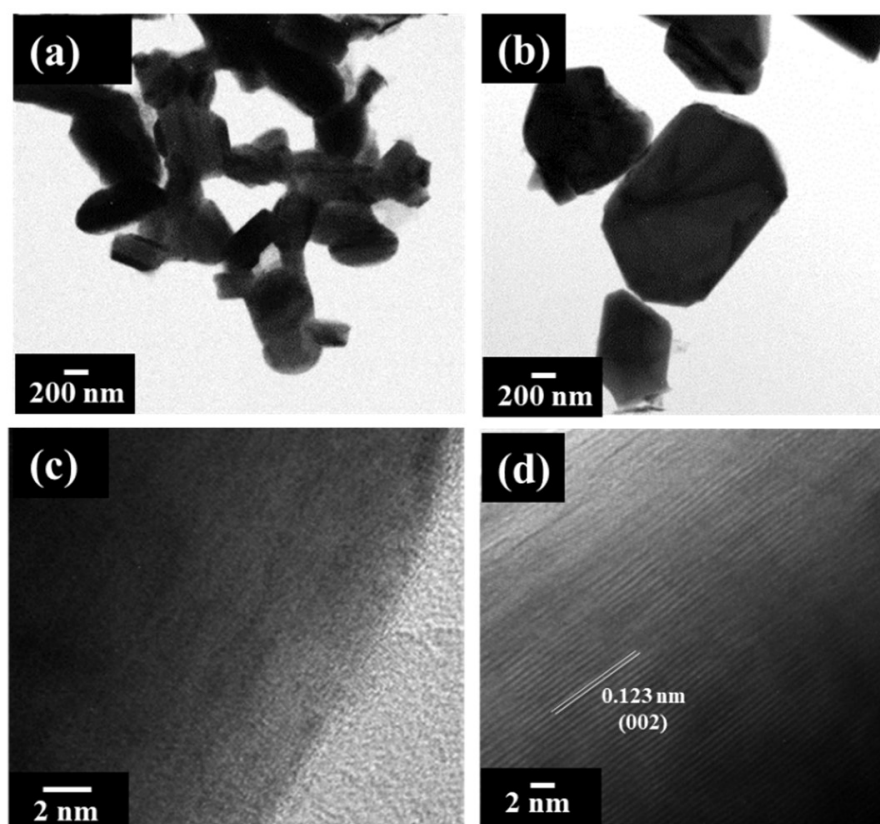


**Figure 4.** TEM images of the (**a**) NaCM-*iB* and (**b**) NaCM-*f*, HRTEM images of the (**c**) NaCM-*iB* and (**d**) NaCM-*f* samples.

XPS analysis of the NaCM-*iB* cathode was carried out to understand the chemical states of the constituent elements. The survey spectrum (Figure 5a) exhibited peaks corresponding

to the elements Na, Mn, Co, O, and C. The high-resolution XPS spectrum of Na1s in Figure 5b consists of a single peak centered at 1070.1 eV, indicating $Na^+$ species [36]. The Mn2p spectrum comprises two broad peaks centered at 641.8 and 653.2 eV, denoting the $Mn2p_{3/2}$ and $Mn2p_{1/2}$ states (Figure 5c). These major peaks could be deconvoluted into the peaks centered at 641.5 eV and 653.2 eV corresponding to the $Mn^{3+}$ state and at 642.9 eV and 654.8 eV, indicating the $Mn^{4+}$ state [24,37]. Thus, the coexistence of the $Mn^{4+}$ and $Mn^{3+}$ oxidation states is confirmed in the NaCM-*iB* cathode. Figure 5d shows the Co2p spectrum of the cathode material. Two peaks centered at 779.7 eV and 794.8 eV were observed in the Co2p spectrum corresponding to the $Co2p_{3/2}$ and $Co2p_{1/2}$ states in the cathode material [37]. The O1s spectrum in Figure 5e is composed of two individual peaks around 528.9 and 531.1 eV. The first peak centered at 528.9 eV denotes the bonding of $O_2^{2-}$ anions in the crystal lattice with metallic species [38]. The peak at 531.1 eV can be attributed to the lattice oxygen with coordination deficiency [38]. Figure 5f shows the C1s spectrum. The C1s component observed at 284.1 eV in the survey spectrum can be attributed to the adventitious carbon; accordingly, all the peaks were referenced to this value [39]. The peaks at 285.0 and 287.9 eV were ascribed to the surface defect arising from the C–O and carboxyl (C=O) groups, respectively [39].
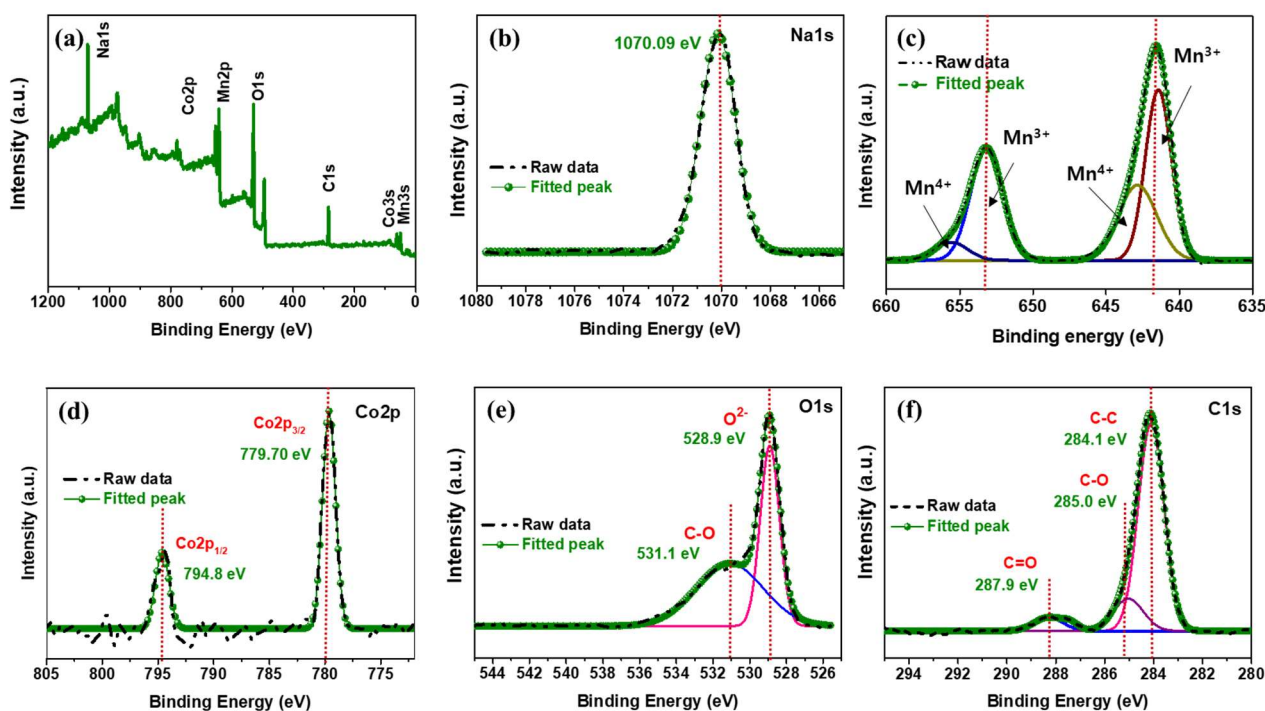


**Figure 5.** XPS spectra of the NaCM-*iB* cathode material: (**a**) survey spectrum and high-resolution (**b**) Na1s, (**c**) Mn2p, (**d**) Co2p, (**e**) O1s, and (**f**) C1s spectra.

The electrochemical properties of the NaCM-*iB* cathode were analyzed in detail via GCD studies vs. $Na/Na^+$. Figure 6a,b shows the voltage profiles of the NaCM-*iB* and NaCM-*f* cathodes at a current density of 50 mA $g^{-1}$. It should be noted that both cathodes displayed a single voltage plateau centered around 2.25 V. However, the initial charging capacity of both synthesized cathode materials was much lower compared to the discharge capacity commonly observed in previous works [23,40]. The low initial capacity can be attributed to a structure-related limitation of this material that allows the de-insertion of Na ions only until the Na stoichiometry reaches 0.44 with this initial composition [41]. Upon further discharge, when the structure is filled with sodium ions, they can be extracted from the second cycle onwards during the charging process, increasing capacity. It is to be noted that the NaCM-*iB* cathode exhibited a high initial discharge capacity of 180.2 mAh $g^{-1}$, while the discharge capacity of the NaCM-*f* cathode was limited to 155.3 mAh $g^{-1}$. Both

samples showed an irreversible loss of the second charge capacity, but the NaCM-*iB* cathode maintained high capacity retention, retaining almost 89% of the initial discharge capacity. CV scan of the NaCM-*iB* cathode was carried out at 0.01 mV s$^{-1}$, as shown in Figure S4. The CV curves exhibited reduction and oxidation peaks corresponding to the complex redox processes of Co and Mn with mixed valence states (Mn$^{3+/4+}$ transitions below 2.75 V and Co$^{2+/3+}$ transitions beyond 3.0 V) in line with previous reports [42]. The trend of irreversible capacity loss in the first cycle was also observed in the CV curves, which stabilized from the second cycle onwards. The comparative cycle performance of the NaCM-*iB* and NaCM-*f* cathodes is shown in Figure 6c. The capacity of the NaCM-*f* cathode deteriorated drastically in the initial cycles, as commonly observed in previous works [23,24,40]. At the same time, the NaCM-*iB* cathode maintained a stable cycling performance, retaining a high discharge capacity of 151.9 mAh g$^{-1}$ after 130 cycles and a low capacity decay rate (0.12% per cycle), indicating high reversibility. At the same time, the observed capacity improvement of NaCM-*iB* compared with flake-like NaCM-*f* could be attributed to the short diffusion lengths achieved with one-dimensional morphology and particle downsizing. This can promote rapid ion/electron transport pathways and ensure complete sodiation/desodiation in the NaCM-*iB* cathode, leading to capacity enhancement.
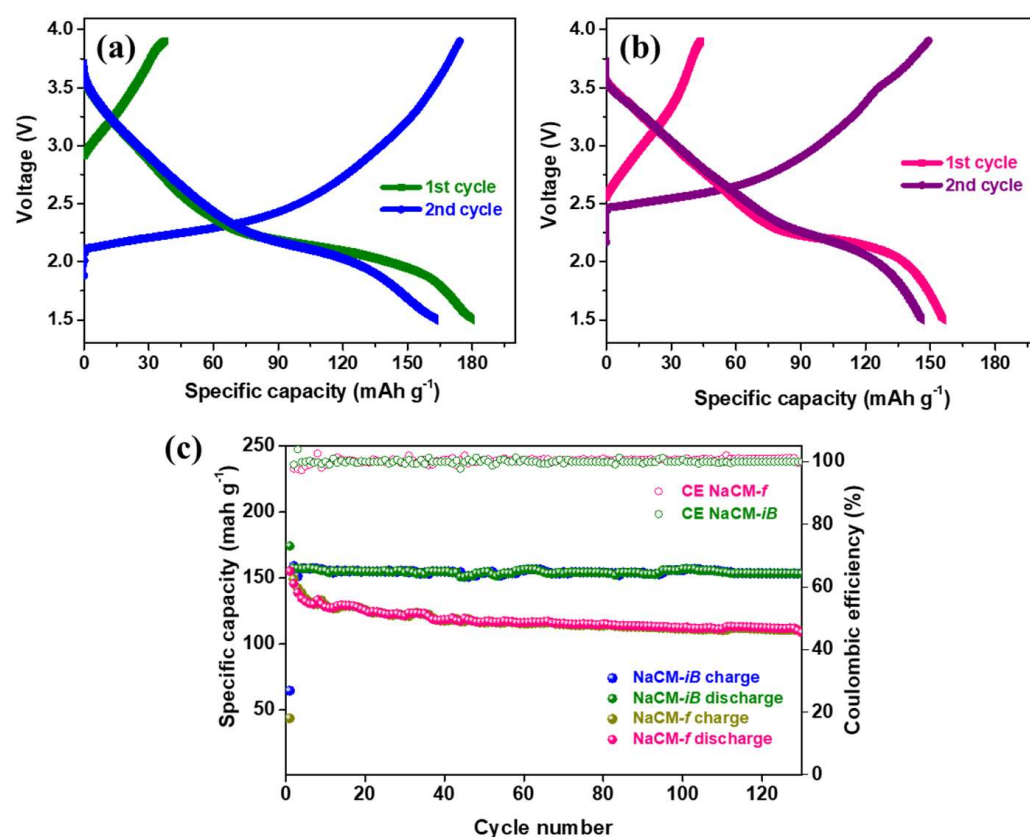


**Figure 6.** Voltage profiles of the (**a**) NaCM-*iB* and (**b**) NaCM-*f* electrodes vs. Na/Na$^+$ (**c**) cycle performance of the NaCM-*iB* and NaCM-*f* electrodes.

The rate performance of the cathode materials was investigated by sequentially increasing the current rate from 150 mA g$^{-1}$ to 5000 mA g$^{-1}$. Figure 7a shows the rate capability tests of both NaCM-*iB* and NaCM-*f* vs. Na/Na$^+$. It can be noted that the NaCM-*iB* cathode exhibited a better rate performance compared to the NaCM-*f* cathode. At 5000 mA g$^{-1}$, the NaCM-*iB* cathode delivered a high capacity of 70 mAh g$^{-1}$. This exceptional performance of the NaCM-*iB* cathode can be attributed to the efficient and fast Na$^+$ transport via the 1D cathode structure.
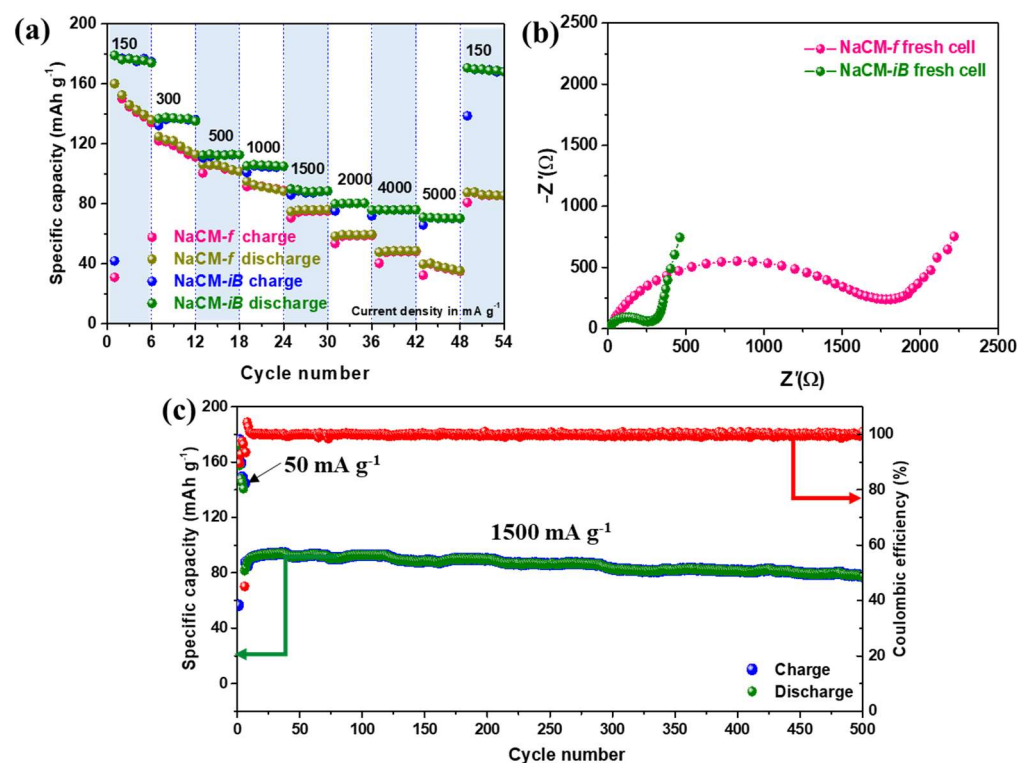
**Figure 7.** (**a**) Rate performance and (**b**) EIS spectra of the NaCM-*iB* and NaCM-*f* electrodes, (**c**) long-term cycling of the NaCM-*iB* cathode.

The EIS spectra of the NaCM-*iB* and NaCM-*f* cells recorded before cycling (Figure 7b) exhibited a similar pattern, consisting of a semicircle at the high-to-medium frequency region. The x-intercept of the semicircle observed at the mid-frequency region indicates the charge transfer resistance ($R_{ct}$), and the straight line in the low-frequency region is the Warburg element ($W$), related to the diffusion process. However, it can be noted that the $R_{ct}$ of the NaCM-*iB* cathode was much lower (almost 20 times lower) than that of the NaCM-*f* cathode. Further, the slope of the $W$ was also comparatively lower in the case of the NaCM-*iB* cathode, indicating favorable Na$^+$ diffusion characteristics. The long-term electrochemical performance of the NaCM-*iB* cathode was evaluated at 1500 mA g$^{-1}$ after precycling the cells at a lower current density of 50 mA g$^{-1}$ for the initial five cycles. Upon switching to a higher current rate, the NaCM-*iB* cathode displayed a lower initial discharge capacity, which later stabilized to 92.1 mAh g$^{-1}$ from the 16th cycle onwards. An excellent capacity of 78.3 mAh g$^{-1}$ (Figure 7c) towards the end of 500 cycles, with a capacity retention of 85.0%, was observed. The capacity retention was calculated from the 16th cycle onwards to ensure a better reflection of the capacity fade. The average coulombic efficiency during the long-term cycling was calculated to be 99.97 ± 0.037.

Following this, additional investigations were carried out to understand the excellent cycle performance achieved by the NaCM-*iB* cathode. XPS analysis of the NaCM-*iB* electrode involving the Na1s, Mn2p, and Co2p spectra is provided in Figure 8. Post-cycling ex-situ XPS analysis revealed that the Mn2p$_{3/2}$ spectra of the NaCM-*iB* electrode were shifted to lower binding energies compared to the pristine NaCM-*iB* electrode after charging to 3.9 V (Figure 8b). This observation agrees with previous reports, confirming the increase in Mn$^{3+}$ species as a result of the partial replacement of Mn$^{4+}$ with Mn$^{3+}$ upon charging to 3.9 V [43,44]. Similarly, the Co2p$_{3/2}$ spectra in Figure 8c show that the binding energy of Co shifted to higher energy values, confirming the electrochemical oxidation of Co$^{2+}$ to Co$^{3+}$ in the sodium cells [44]. Partial Co doping can replace the Mn$^{3+}$ in P2-Na$_x$MnO$_2$ and reduce the structural degradation due to the Jahn–Teller distortion, improving the cycling stability [45]. However, the NaCM-*iB* and NaCM-*f* electrodes exhibited similar Mn2p$_{3/2}$

and Co2p$_{3/2}$ spectra upon charging to 3.9 V, implying similar chemical characteristics. Thus, it can be confirmed that the only variation between these composites otherwise is the morphology. Hence, we conclude that the superior electrochemical performance of the NaCM-*iB* cathode over NaCM-*f* is due to the unique interconnected bead-like morphology that helps lower Na$^+$ diffusion lengths, ensuring fast and efficient Na$^+$ transport within the electrode structure.
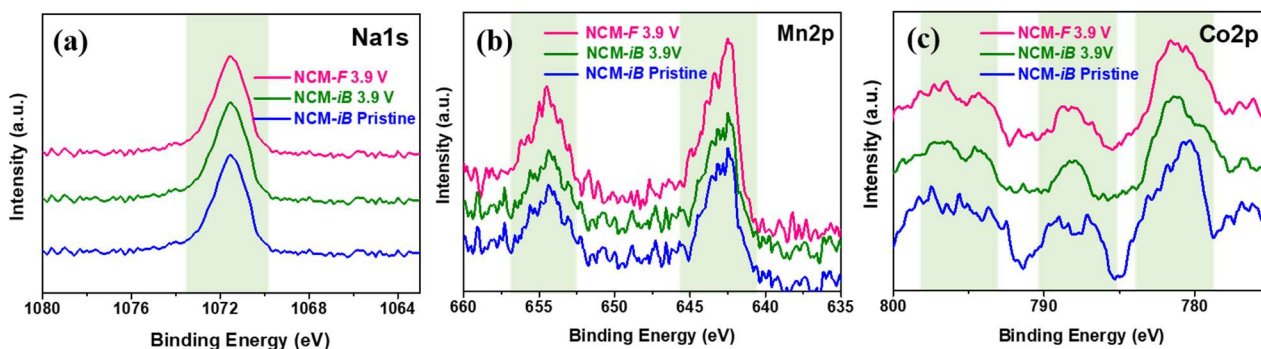


**Figure 8.** Ex-situ XPS spectra of the NaCM-*iB* and NaCM-*f* cathodes: (**a**) Na1s, (**b**) Mn2p, and (**c**) Co2p spectra.

We also assembled Na-ion full cells combining the NaCM-*iB* cathode with a CNF anode prepared in-house (see Supporting Information) to demonstrate practical application. Interestingly, the preliminary investigation of NaCM-*iB*||CNF full cells revealed a promising electrochemical performance, retaining a capacity of 96.3 mAh g$^{-1}$ at 300 mA g$^{-1}$ even after 100 cycles (Figure S6). Additionally, the lighting of green LED was also successfully demonstrated with an NaCM-*iB*||CNF coin cell (Figure S5, inset), indicating excellent prospects for applications.

## 4. Conclusions

An interconnected bead-like P2 manganese oxide with partial Co doping, Na$_x$Co$_y$Mn$_{1-y}$O$_2$ (x = 0.66, y = 0.1), was successfully synthesized by means of a rational PVP-assisted electrospinning/heat treatment process as a high-rate cathode material for SIBs. The electrospun cathode exhibited a superior discharge capacity of 180.0 mAh g$^{-1}$ (50 mA g$^{-1}$) and demonstrated excellent cyclability, retaining 78.3 mAh g$^{-1}$ (1500 mAh g$^{-1}$) even after 500 cycles. The strategy of simultaneous Co doping and 1D nanostructuring could alleviate the issue of the Jahn–Teller distortion in the material and facilitate rapid Na$^+$ transport, resulting in high-rate Na$^+$ storage. Full batteries assembled with the synthesized NaCM-*iB* cathode and a CNF anode also exhibited a promising cycle performance, retaining 96.3 mAh g$^{-1}$ even after 100 cycles.

**Author Contributions:** A.K.H.: conceptualization, methodology, investigation, writing—original draft preparation; M.K.S.: methodology, validation; J.-H.K.: writing—review and editing; Y.L.:

## References

1. Tarascon, J.M.; Armand, M. Issues and challenges facing rechargeable lithium batteries. *Nature* **2001**, *414*, 359–367. [CrossRef]
2. Armand, M.; Tarascon, J.M. Building better batteries. *Nature* **2008**, *451*, 652–657. [CrossRef]
3. Tarascon, J.M. Is lithium the new gold? *Nat. Chem.* **2010**, *2*, 510. [CrossRef]
4. Kim, S.-W.; Seo, D.-H.; Ma, X.; Ceder, G.; Kang, K. Electrode Materials for Rechargeable Sodium-Ion Batteries: Potential Alternatives to Current Lithium-Ion Batteries. *Adv. Energy Mater.* **2012**, *2*, 710–721. [CrossRef]
5. Wang, L.P.; Yu, L.; Wang, X.; Srinivasan, M.; Xu, Z.J. Recent developments in electrode materials for sodium-ion batteries. *J. Mater. Chem. A* **2015**, *3*, 9353–9378. [CrossRef]
6. Jiang, Y.; Yu, S.; Wang, B.; Li, Y.; Sun, W.; Lu, Y.; Yan, M.; Song, B.; Dou, S. Prussian Blue@C Composite as an Ultrahigh-Rate and Long-Life Sodium-Ion Battery Cathode. *Adv. Funct. Mater.* **2016**, *26*, 5315–5321. [CrossRef]
7. Yue, Y.; Binder, A.J.; Guo, B.; Zhang, Z.; Qiao, Z.A.; Tian, C.; Dai, S. Mesoporous Prussian blue analogues: Template-free synthesis and sodium-ion battery applications. *Angew. Chem.* **2014**, *53*, 3134–3137. [CrossRef]
8. Fan, X.; Hu, E.; Ji, X.; Zhu, Y.; Han, F.; Hwang, S.; Liu, J.; Bak, S.; Ma, Z.; Gao, T.; et al. High energy-density and reversibility of iron fluoride cathode enabled via an intercalation-extrusion reaction. *Nat. Commun.* **2018**, *9*, 2324. [CrossRef]
9. Euchner, H.; Clemens, O.; Reddy, M.A. Unlocking the potential of weberite-type metal fluorides in electrochemical energy storage. *Npj Comput. Mater.* **2019**, *5*, 31. [CrossRef]
10. Ni, Q.; Bai, Y.; Wu, F.; Wu, C. Polyanion-Type Electrode Materials for Sodium-Ion Batteries. *Adv. Sci.* **2017**, *4*, 1600275. [CrossRef]
11. Barpanda, P.; Lander, L.; Nishimura, S.-I.; Yamada, A. Polyanionic Insertion Materials for Sodium-Ion Batteries. *Adv. Energy Mater.* **2018**, *8*, 1703055. [CrossRef]
12. Han, M.H.; Gonzalo, E.; Singh, G.; Rojo, T. A comprehensive review of sodium layered oxides: Powerful cathodes for Na-ion batteries. *Energy Environ. Sci.* **2015**, *8*, 81–102. [CrossRef]
13. Chagas, L.G.; Buchholz, D.; Vaalma, C.; Wu, L.; Passerini, S. P-type $Na_xNi_{0.22}Co_{0.11}Mn_{0.66}O_2$ materials: Linking synthesis with structure and electrochemical performance. *J. Mater. Chem. A* **2014**, *2*, 20263–20270. [CrossRef]
14. Hasa, I.; Buchholz, D.; Passerini, S.; Scrosati, B.; Hassoun, J. High Performance $Na_{0.5}[Ni_{0.23}Fe_{0.13}Mn_{0.63}]O_2$ Cathode for Sodium-Ion Batteries. *Adv. Energy Mater.* **2014**, *4*, 1400083. [CrossRef]
15. Delmas, C.; Fouassier, C.; Hagenmuller, P. Structural classification and properties of the layered oxides. *Phys. B+C* **1980**, *99*, 81–85. [CrossRef]
16. Yabuuchi, N.; Kajiyama, M.; Iwatate, J.; Nishikawa, H.; Hitomi, S.; Okuyama, R.; Usui, R.; Yamada, Y.; Komaba, S. P2-type $Na_x[Fe_{1/2}Mn_{1/2}]O_2$ made from earth-abundant elements for rechargeable Na batteries. *Nat. Mater.* **2012**, *11*, 512–517. [CrossRef]
17. Mortemard de Boisse, B.; Carlier, D.; Guignard, M.; Delmas, C. Structural and Electrochemical Characterizations of P2 and New O3-$Na_xMn_{1-y}Fe_yO_2$ Phases Prepared by Auto-Combustion Synthesis for Na-Ion Batteries. *J. Electrochem. Soc.* **2013**, *160*, A569–A574. [CrossRef]
18. Luo, C.; Langrock, A.; Fan, X.; Liang, Y.; Wang, C. P2-type transition metal oxides for high performance Na-ion battery cathodes. *J. Mater. Chem. A* **2017**, *5*, 18214–18220. [CrossRef]
19. Kalluri, S.; Seng, K.H.; Pang, W.K.; Guo, Z.; Chen, Z.; Liu, H.K.; Dou, S.X. Electrospun P2-type $Na_{2/3}(Fe_{1/2}Mn_{1/2})O_2$ hierarchical nanofibers as cathode material for sodium-ion batteries. *ACS Appl. Mater. Interfaces* **2014**, *6*, 8953–8958. [CrossRef]
20. Li, S.; Zhang, Y.; Lei, K.; Yang, Q.; Liu, Z.; Jiang, K.; Li, F.; Lu, Q.; Mikhailova, D.; Zheng, S. Na+/vacancy disordered manganese-based oxide cathode with ultralow strain enabled by tuning charge distribution. *J. Mater. Chem. A* **2022**, *10*, 10391–10399. [CrossRef]
21. Baster, D.; Zając, W.; Kondracki, Ł.; Hartman, F.; Molenda, J. Improvement of electrochemical performance of $Na_{0.7}Co_{1-y}Mn_yO_2$—Cathode material for rechargeable sodium-ion batteries. *Solid State Ion.* **2016**, *288*, 213–218. [CrossRef]
22. Hemalatha, K.; Jayakumar, M.; Prakash, A.S. Influence of the manganese and cobalt content on the electrochemical performance of P2-$Na_{0.67}Mn_xCo_{1-x}O_2$ cathodes for sodium-ion batteries. *Dalton Trans.* **2018**, *47*, 1223–1232. [CrossRef] [PubMed]
23. Bucher, N.; Hartung, S.; Franklin, J.B.; Wise, A.M.; Lim, L.Y.; Chen, H.-Y.; Weker, J.N.; Toney, M.F.; Srinivasan, M. P2–$Na_xCo_yMn_{1-y}O_2$ (y = 0, 0.1) as Cathode Materials in Sodium-Ion Batteries—Effects of Doping and Morphology To Enhance Cycling Stability. *Chem. Mater.* **2016**, *28*, 2041–2051. [CrossRef]
24. Fu, C.C.; Wang, J.; Li, Y.; Liu, G.; Deng, T. Explore the effect of Co Doping on P2-$Na_{0.67}MnO_2$ prepared by hydrothermal method as cathode materials for sodium ion batteries. *J. Alloy. Compd.* **2022**, *918*, 165569. [CrossRef]

25.  Li, H.; Bai, Y.; Wu, F.; Ni, Q.; Wu, C. Na$_3$V$_2$(PO$_4$)$_3$/C nanorods as advanced cathode material for sodium ion batteries. *Solid State Ion.* **2015**, *278*, 281–286. [CrossRef]

26.  Mai, L.; Xu, L.; Han, C.; Xu, X.; Luo, Y.; Zhao, S.; Zhao, Y. Electrospun ultralong hierarchical vanadium oxide nanowires with high performance for lithium ion batteries. *Nano Lett.* **2010**, *10*, 4750–4755. [CrossRef]

27.  Haridas, A.K.; Heo, J.; Li, X.; Ahn, H.-J.; Zhao, X.; Deng, Z.; Agostini, M.; Matic, A.; Ahn, J.-H. A flexible and free-standing FeS/sulfurized polyacrylonitrile hybrid anode material for high-rate sodium-ion storage. *Chem. Eng. J.* **2019**, *385*, 123453. [CrossRef]

28.  Li, X.; Chen, W.; Qian, Q.; Huang, H.; Chen, Y.; Wang, Z.; Chen, Q.; Yang, J.; Li, J.; Mai, Y.W. Electrospinning-Based Strategies for Battery Materials. *Adv. Energy Mater.* **2020**, *11*, 2000845. [CrossRef]

29.  Ho, Y.-C.; Chung, S.-H. A design of the cathode substrate for high-loading polysulfide cathodes in lean-electrolyte lithium-sulfur cells. *Chem. Eng. J.* **2021**, *422*, 130363. [CrossRef]

30.  Barbosa, J.C.; Correia, D.M.; Fidalgo-Marijuan, A.; Gonçalves, R.; Fernandes, M.; de Zea Bermudez, V.; Silva, M.M.; Lanceros-Mendez, S.; Costa, C.M. Sustainable Lithium-Ion Battery Separators Based on Poly(3-Hydroxybutyrate-Co-Hydroxyvalerate) Pristine and Composite Electrospun Membranes. *Energy Technol.* **2021**, *10*, 2100761. [CrossRef]

31.  Joshi, B.; Samuel, E.; Kim, Y.-i.; Yarin, A.L.; Swihart, M.T.; Yoon, S.S. Progress and potential of electrospinning-derived substrate-free and binder-free lithium-ion battery electrodes. *Chem. Eng. J.* **2022**, *430*, 132876. [CrossRef]

32.  Haridas, A.K.; Sharma, C.S.; Rao, T.N. Caterpillar-like sub-micron LiNi$_{0.5}$Mn$_{1.5}$O$_4$ structures with site disorder and excess Mn$^{3+}$ as high performance cathode material for lithium ion batteries. *Electrochim. Acta* **2016**, *212*, 500–509. [CrossRef]

33.  Fu, B.; Zhou, X.; Wang, Y. High-rate performance electrospun Na$_{0.44}$MnO$_2$ nanofibers as cathode material for sodium-ion batteries. *J. Power Sources* **2016**, *310*, 102–108. [CrossRef]

34.  Li, J.-Y.; Lü, H.-Y.; Zhang, X.-H.; Xing, Y.-M.; Wang, G.; Guan, H.-Y.; Wu, X.-L. P2-type Na$_{0.53}$MnO$_2$ nanorods with superior rate capabilities as advanced cathode material for sodium ion batteries. *Chem. Eng. J.* **2017**, *316*, 499–505. [CrossRef]

35.  Zhao, X.; Liu, Y.; Manuel, J.; Chauhan, G.S.; Ahn, H.J.; Kim, K.W.; Cho, K.K.; Ahn, J.H. Nitrogen-Doped Mesoporous Carbon: A Top-Down Strategy to Promote Sulfur Immobilization for Lithium-Sulfur Batteries. *ChemSusChem* **2015**, *8*, 3234–3241. [CrossRef]

36.  Kumar Gupta, N.; Bae, J.; Soo Kim, K. Metal-organic framework-derived NaMn$_x$O$_y$ hexagonal microsheets for superior adsorptive-oxidative removal of hydrogen sulfide in ambient conditions. *Chem. Eng. J.* **2022**, *427*, 130909. [CrossRef]

37.  Chen, X.; Zhou, X.; Hu, M.; Liang, J.; Wu, D.; Wei, J.; Zhou, Z. Stable layered P3/P2 Na$_{0.66}$Co$_{0.5}$Mn$_{0.5}$O$_2$ cathode materials for sodium-ion batteries. *J. Mater. Chem. A* **2015**, *3*, 20708–20714. [CrossRef]

38.  Li, Y.; Wu, X.; Wang, S.; Wang, W.; Xiang, Y.; Dai, C.; Liu, Z.; He, Z.; Wu, X. Surfactant-assisted solvothermal synthesis of NiCo$_2$O$_4$ as an anode for lithium-ion batteries. *RSC Adv.* **2017**, *7*, 36909–36916. [CrossRef]

39.  Haridas, A.K.; Sadan, M.K.; Liu, Y.; Jung, H.Y.; Lee, Y.; Ahn, H.-J.; Ahn, J.-H. Simple and scalable gelatin-mediated synthesis of a novel iron sulfide/graphitic carbon nanoarchitecture for sustainable sodium-ion storage. *J. Alloy. Compd.* **2022**, *928*, 167125. [CrossRef]

40.  Zhou, Y.-T.; Sun, X.; Zou, B.-K.; Liao, J.-Y.; Wen, Z.-Y.; Chen, C.-H. Cobalt-substituted Na$_{0.44}$Mn$_{1-x}$Co$_x$O$_2$: Phase evolution and a high capacity positive electrode for sodium-ion batteries. *Electrochim. Acta* **2016**, *213*, 496–503. [CrossRef]

41.  Bucher, N.; Hartung, S.; Nagasubramanian, A.; Cheah, Y.L.; Hoster, H.E.; Madhavi, S. Layered Na$_x$MnO$_{2+z}$ in sodium ion batteries-influence of morphology on cycle performance. *ACS Appl. Mater. Interfaces* **2014**, *6*, 8059–8065. [CrossRef]

42.  Wang, X.; Tamaru, M.; Okubo, M.; Yamada, A. Electrode Properties of P2–Na$_{2/3}$Mn$_y$Co$_{1-y}$O$_2$ as Cathode Materials for Sodium-Ion Batteries. *J. Phys. Chem. C* **2013**, *117*, 15545–15551. [CrossRef]

43.  Wang, C.; Liu, L.; Zhao, S.; Liu, Y.; Yang, Y.; Yu, H.; Lee, S.; Lee, G.H.; Kang, Y.M.; Liu, R.; et al. Tuning local chemistry of P2 layered-oxide cathode for high energy and long cycles of sodium-ion battery. *Nat. Commun.* **2021**, *12*, 2256. [CrossRef]

44.  Luo, R.; Wu, F.; Xie, M.; Ying, Y.; Zhou, J.; Huang, Y.; Ye, Y.; Li, L.; Chen, R. Habit plane-driven P2-type manganese-based layered oxide as long cycling cathode for Na-ion batteries. *J. Power Sources* **2018**, *383*, 80–86. [CrossRef]

45.  Konarov, A.; Kim, H.J.; Voronina, N.; Bakenov, Z.; Myung, S.T. P2-Na$_{2/3}$MnO$_2$ by Co Incorporation: As a Cathode Material of High Capacity and Long Cycle Life for Sodium-Ion Batteries. *ACS Appl. Mater. Interfaces* **2019**, *11*, 28928–28933. [CrossRef]